Dynamic Coupling and Cooperative Control for Multi-paralleled Doubly Fed Induction Generator Wind Farms during Symmetrical Low Voltage Ride-through in a Weak Grid

Lei Guan and Jun Yao

***Abstract*—In multi-fed grid-connected systems, there are complex dynamic interactions between different pieces of equipment. Particularly in situations of weak-grid faults, the dynamic coupling between equipment becomes more pronounced. This may cause the system to experience small-signal instability during the fault steady-state. In this paper, multi-paralleled doubly fed induction generator (DFIG)-based wind farms (WFs) are taken as an example to study the dynamic coupling within a multi-fed system during fault steady-state of symmetrical low voltage ride-through (LVRT) in a weak grid. The analysis reveals that the dynamic coupling between WFs will introduce a damping shift to each WF. This inevitably affects the system's dynamic stability and brings the risk of small-signal instability during fault steady-state in LVRT scenarios. Increasing the distance to fault location and fault severity will exacerbate the dynamic coupling between WFs. Because of the dynamic coupling, adjusting the control state of one WF will affect the stability of the remaining WFs in the system. Hence, a cooperative control strategy for multi-paralleled DFIG WFs is proposed to improve dynamic stability during LVRT. The analysis and the effectiveness of the proposed control strategy are verified by modal analysis and simulation.**

***Index Terms*—Doubly fed induction generator (DFIG), wind farms (WFs), dynamic stability, low voltage ride through (LVRT), weak grid, dynamic coupling.**

NOMENCLATURE

A. Variables

θ_r, ω_r	Angle and angular frequency of rotor
U_{PCC}	PCC voltage
Z_t	Impedance of transmission line between WF and PCC
Z_L	Impedance of transmission line between PCC and grid

B. Subscripts

d, *q*	*dq*-axis components
s, r, g	Stator-, rotor-side and GSC-side quantities
G	Quantities of grid
0	Initial value

C. Superscripts

p*j*	Components in the *j*th PLL detected SRF

I. INTRODUCTION

Because of the growing emphasis on protection of the environment and green energy, an increasing number of renewable energy generation systems (REGs) using doubly fed induction generator (DFIG)-based wind turbines (WTs) have been installed [1]. However, because of the uneven distribution of wind resources, wind farms (WFs) are usually installed far away from the electricity load. This leads to long distance and high impedance characteristics of the transmission line (weak grid characteristics) [2]. Consequently, an increasing proportion of wind farms are integrated into the power system through weak grid connection. This brings significant challenges to the power system, including stability issues when there are faults [3], [4].

Stability issues of wind farms during weak grid faults have received significant attention. From the timescale point of view, power system faults can be divided into two transient stages (fault initiation stage and fault clearance stage) as well as one steady-state stage (fault steady-state) [5]. Therefore, the stability issues include transient stability (large-signal stability) during fault transient stages, and dynamic stability (small-signal stability) during fault steady-state. The transient stability during fault transient stages ensures that the grid-connected system has an equilibrium point in grid

Received: July 1, 2023
Accepted: October 5, 2023
Published Online: May 1, 2024
Jun Yao (corresponding author) is with the State Key Laboratory of Power Transmission Equipment Technology, School of Electrical Engineering, Chongqing University, Chongqing 400044, China (e-mail: jyao@cqu.edu.cn).
DOI: 10.23919/PCMP.2023.000539

fault conditions, a point which can be reached smoothly [6], [7]. On the other hand, during the fault steady-state, the transient components in the system have completely attenuated, and the dynamic stability ensures that the grid-connected system can maintain normal operation at the equilibrium point during the fault steady-state until the fault is cleared [8], [9]. The dynamic stability of the wind farm during the fault steady-state is equally important, and it may also affect the success of the fault ride-through (FRT) operation. Some studies have verified that dynamic instability can indeed occur in grid-connected systems during the fault steady-state in a weak grid, and the fundamental causes for dynamic instability during FRT have also been investigated [8]–[11]. In these studies, it is illustrated that grid-connected power-electronic-based renewable energy generation is more prone to induce small-signal instability during weak grid faults because of changes in the grid structure and control status caused by the faults. Studies [8]–[11] investigate the dynamic stability of an independent grid-connected system during a fault steady-state in a weak grid. In the context of multi-fed grid-connected systems, there exists dynamic interaction behavior due to the integration of various pieces of equipment into a unified system, resulting in new and complex effects. Therefore, conclusions drawn from an independent grid-connected system are not applicable to the dynamic stability analysis of multi-fed grid-connected systems (multiple WFs) during a fault steady-state.

Different from the independent grid-connected system, the dynamic interactions between WFs make the stability of multiple WFs during the fault steady-state in a weak grid fault more complex. [12]–[14] study the dynamic stability of grid-connected WFs and propose a dynamic aggregation method to aggregate a WF containing multiple wind turbine generators (WTGs) into an equivalent single WTG system. In [15], multiple renewable energy generation plants (photovoltaic plants and wind farms) are made equivalent to a multi-fed power electronic grid-connected system by applying the dynamic aggregation modeling method. However, the above research only discusses the stability of the multi-fed grid-connected system under normal conditions, not under fault conditions. Also, the influence of dynamic interactions in a multi-fed grid-connected system on small-signal stability of the overall system has not been thoroughly explored. In [16], [17], it is pointed out that the coupling relationship between multi-paralleled WFs will affect transient stability. Even so, the dynamic stability of multiple WFs during a fault steady-state has not been not investigated.

From the existing research on stability in normal weak grid operation conditions [12]–[15] and the transient stability under weak grid faults [16], [17], it can be seen that the dynamic coupling between WFs is important. Changes in the grid structure and control status caused by faults lead to changes in the dynamic coupling relationship between WFs, and that affects system dynamic stability during the fault steady-state in weak grid faults [17]–[19]. This study focuses on these issues, and the main contributions of this paper are as follows:

1) The dynamic coupling mechanism between DFIG WFs during fault steady-state in LVRT is studied. It reveals that it can bring new instability risk to the multi-WF system during LVRT, and can also reduce the effectiveness of traditional stability improvement control.

2) It points out that a more distant fault location or a more severe fault condition can intensify the dynamic coupling effect and decrease the small-signal stability. In addition, the causes of small-signal instability of multi-paralleled WFs during LVRT are revealed.

3) Because of dynamic coupling, the integration of multiple WFs into a unified system means that modifying the control state of one WF will affect the stability of the remaining WFs in the multi-fed system. A cooperative control strategy is thus proposed to improve the dynamic stability in the circumstances under study.

The rest of the paper is organized as follows. Section II develops the multi-WF system model considering dynamic coupling. In Section III, the influence mechanism of dynamic coupling between WFs and the dynamic stability of multi-paralleled WFs during LVRT are studied. The cooperative control strategy for improving the dynamic stability of multi-paralleled WFs during LVRT is designed in Section IV, while simulation verification is carried out in Section V. Section VI gives the conclusions of the paper.

II. Modeling Considering Dynamic Coupling for Multi-paralleled Wind Farms During Symmetrical LVRT

Figure 1 shows the typical configuration and LVRT strategy of a DFIG-based wind energy conversion system (WECS) [8]–[10]. During LVRT, the wind farm needs to inject corresponding reactive current into the grid according to the degree of voltage sag [20]. The expression of the injected reactive current is given as:

$$I_{\text{gqref}} = 1.5(0.9 - U_{\text{td}}) \tag{1}$$

The WECS will cut off the power control loop and only use the current control loop (CCL) for control during LVRT. A typical PLL structure, as shown in Fig. 2, is used for synchronization between the WECS and grid.

This paper primarily studies the dynamic stability of the fault steady-state, in which the transient fault component has completely attenuated and the system operates at the stable operating point. The crowbar on the rotor side and/or the chopper on the DC side have been deactivated during the fault steady-state. Therefore, referring to the modeling methods on dynamic stability during faults in previous studies [8]–[11], the small-signal model can be obtained by linearizing the

mathematical model at the stable operating point of the fault steady-state. Since a wind farm generally contains the same types of WTs, it is assumed that their control parameters are set to the same values [12], [21].

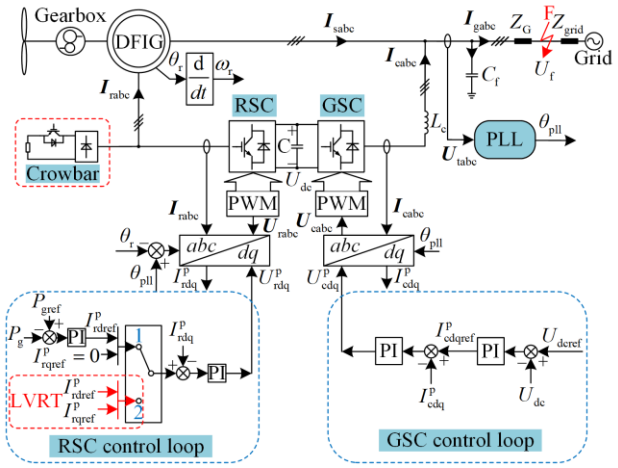

Fig. 1. Control structure diagram of DFIG-based WECS.

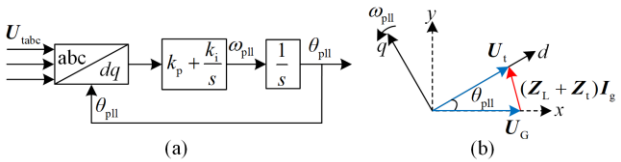

Fig. 2. Structure diagram of PLL.

Compared with a strong grid, the short circuit ratio (SCR) of a weak grid is low, and the transmission line impedance $Z_G = R_G + jX_G$ becomes significant. Therefore, the WF's terminal voltage U_t is affected not only by the fault point voltage U_f, but also by the output current I_g, i.e., $U_t = U_f + I_g Z_G$. The terminal voltage dynamic ΔU_t affects the PLL control performance, and thus the output current dynamic ΔI_g also affects the PLL control performance $\Delta\theta_{pll}$. Hence, in the established model in a weak grid, the impedance of the transmission line should be considered.

Compared to the external transmission lines between the wind farm and the grid, the internal transmission lines in the wind farm can be neglected. Therefore, adopting the dynamic aggregation modeling method in [13] to aggregate WTGs in a wind farm, an individual WF can be considered as a controlled current source regulated by the PLL. From Kirchhoff's law, there is:

$$\boldsymbol{U}_t - \boldsymbol{U}_f = \boldsymbol{I}_g \boldsymbol{Z}_G \tag{2}$$

Because of the PLL dynamics, the dynamic relationship in the system can be expressed as:

$$\begin{cases} \Delta \boldsymbol{U}_t^p = \Delta \boldsymbol{U}_t + j\boldsymbol{U}_{t0}\Delta\theta_{pll} \\ \Delta \boldsymbol{I}_g^p = \Delta \boldsymbol{I}_g + j\boldsymbol{I}_{g0}\Delta\theta_{pll} \end{cases} \tag{3}$$

where the superscript p indicates the quantity in the frame detected by the PLL. Substituting (3) into (2) and subsequently linearizing the resulting expression yield:

$$\begin{aligned} \Delta U_{tq}^p = (R_G I_{gd0} + X_G I_{gq0})\Delta\theta_{pll} - U_{td0}\Delta\theta_{pll} + \\ X_G \Delta I_{gd}^p + R_G \Delta I_{gq}^p \end{aligned} \tag{4}$$

Some studies have investigated the dynamic stability of single DFIG-based REGS during symmetric LVRT [8]–[10]. The results show that the damping of the PLL dominant mode of DFIG-based REGS in a symmetric LVRT will become weaker or even shift to a negative value, i.e., the PLL mode is the dominant mode of single DFIG-based REGS during symmetric faults in a weak grid. However, for a multi-fed power electronic grid-connected system composed of multiple DFIG WFs, the dynamic coupling behavior between WFs will bring in new influence on stability. In particular, the effect of this dynamic coupling may become more significant during LVRT.

The main circuit topology of n DFIG WFs in parallel connection is illustrated in Fig. 3. It is seen that the DFIG WFs are respectively connected to the point of common coupling (PCC) through n transmission lines $\boldsymbol{Z}_{t1}$ to $\boldsymbol{Z}_{tn}$, which are then connected to the fault location $\boldsymbol{U}_f$ and grid $\boldsymbol{U}_G$ through the common transmission line $\boldsymbol{Z}_L$ and $\boldsymbol{Z}_{grid}$. Thus, $\boldsymbol{Z}_G = R_G + jX_G = (R_t + R_L) + j(X_t + X_L)$, and from Kirchhoff's law, there are:

$$\boldsymbol{I}_G = \sum_{i=1}^{n} \boldsymbol{I}_{gi} \tag{5}$$

$$\boldsymbol{U}_{pcc} - \boldsymbol{U}_f = \boldsymbol{I}_G \boldsymbol{Z}_L \tag{6}$$

$$\boldsymbol{U}_{ti} - \boldsymbol{U}_{pcc} = \boldsymbol{I}_{gi} \boldsymbol{Z}_{ti} \tag{7}$$

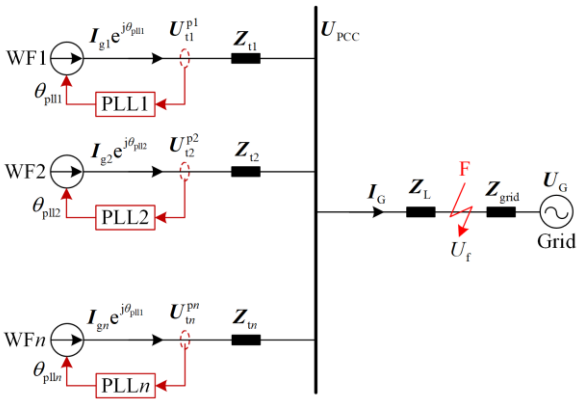

Fig. 3. Equivalent circuit of DFIG WFs in parallel connection.

Since the n DFIG WFs are respectively synchronized with the grid by n independent PLL, there are n independent dq-axis synchronous reference frames (SRF) in the system detected by the n PLL. The relationship between these n dq-axis SRF and the whole system's unified reference XY frame (the orientation of U_f is defined as the direction of X-axis) is shown in Fig. 4,

where the angle between the *k*th PLL-detected *dq*-axis SRF and the *XY* frame is represented by $\theta_{\text{pll}k}$.

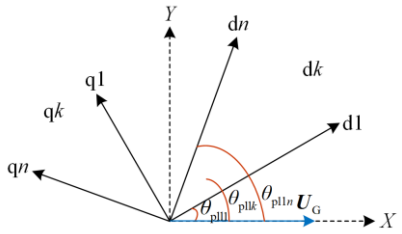

Fig. 4. Relationship between *n* PLL-detected SRFs and the *XY* frame.

Combining (5)–(7), the *q*-axis terminal voltage dynamic of the *k*th DFIG WF can be obtained as:

$$\Delta U_{\text{tq}k}=(R_{\text{t}k}I_{gkd0}+X_{\text{t}k}I_{gkq0})\Delta\theta_{\text{pll}k}+X_{\text{t}k}\Delta I^{\text{p}}_{gkd}+R_{\text{t}k}\Delta I^{\text{p}}_{gkq}+\sum_{j=1}^{n}\left[(R_{\text{L}}I_{gjd0}+X_{\text{L}}I_{gjq0})\Delta\theta_{\text{pll}j}+X_{\text{L}}\Delta I^{\text{p}}_{gjd}+R_{\text{L}}\Delta I^{\text{p}}_{gjq}\right] \tag{8}$$

where $\Delta I^{\text{p}}_{\text{g}}$ is the output current dynamic. From (8), it can be seen that the *k*th DFIG WF's terminal voltage is dynamically coupled with the other *n*-1 paralleled-connected WFs during LVRT. This is because the output currents of the *n* WFs are integrated to the PCC and then are jointly delivered to the faulted grid through the common transmission line $\boldsymbol{Z}_{\text{L}}$. So the output current dynamics of any WF will affect the PCC voltage U_{PCC} and other WFs' terminal voltage $U_{\text{t}k}$. Therefore, the respective control systems of the multi-paralleled WFs are dynamically coupled to each other during LVRT.

Because of the dynamic coupling behavior of the multi-paralleled DFIG WFs during LVRT, the stability of the parallel-connected WFs is influenced by each WF. If one of the WFs is dynamically destabilized during LVRT, its destabilization current will cause fluctuation in the PCC voltage $\boldsymbol{U}_{\text{PCC}}$. Consequently, the oscillating $\boldsymbol{U}_{\text{PCC}}$ will result in oscillations of other WFs' terminal voltage $\boldsymbol{U}_{\text{t}k}$ during LVRT. This in turn affects the dynamic performance and the output current dynamic of each WF.

Here, the small-signal state-space equation of each individual DFIG WF during LVRT is obtained by the modeling method in [8]. The small-signal model of each individual DFIG WF is then combined by (5)–(7) to obtain the entire dynamic model of the multi-paralleled WF system.

From modal analysis, the primary poles of the multi-paralleled WFs during LVRT are still dominated by the PLL modal of each WF. However, the dynamic coupling between WFs during LVRT will influence the position of poles dominated by the PLL modal.

III. Dynamic Coupling Analysis for Multi-paralleled Wind Farms

From [8], it is evident that as the fault location moves farther away or when voltage dips become more severe, the damping of the PLL dominant modal of individual WFs decreases, leading to a less stable overall system. In the following, the effect of the fault location and fault severity on the dynamic coupling between WFs and the dynamic stability of multi-paralleled DFIG WFs is studied.

A. Dynamic Coupling between WFs

Figure 5 illustrates the multi-paralleled DFIG WFs consisting of the *j*th and *k*th WFs [19], [23]. In Fig. 5, superscript *pj* or *pk* indicates the quantity in the frame detected by the PLL of the *j*th WF or *k*th WF. $\Delta U^{\text{pj}}_{\text{t}j}$ indicates the *j*th WF's terminal voltage dynamic in the frame detected by the PLL of the *j*th WF, whereas $\Delta U^{\text{pk}}_{\text{t}k}$ indicates the *k*th WF's terminal voltage dynamic in the frame detected by the PLL of the *k*th WF.

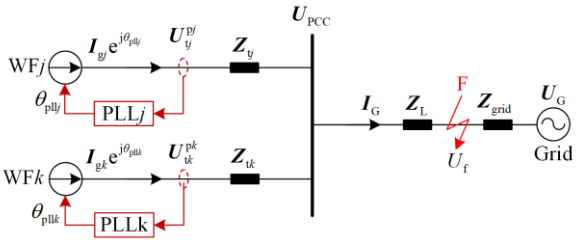

Fig. 5. Multi-paralleled DFIG WFs system consisting of only two WFs.

We assume that the *j*th WF is farther way from the fault location than the *k*th WF, i.e., $\boldsymbol{Z}_{\text{t}j}>\boldsymbol{Z}_{\text{t}k}$, while the remaining parameters of these two WFs are similar. Then, the small-signal state-space model of the two DFIG WFs under LVRT can be established using the modeling method in [8]. It should be noted that the dynamic coupling between the multi-paralleled DFIG WFs is considered in the established model. The influence of the dynamic coupling between WFs on the whole system dynamic stability can be studied by adjusting the coefficients associated with the coupling terms in the small-signal state-space matrix.

Figure 6 compares the PLL dominant poles of the 2-WF system with and without considering the dynamic coupling effect between WFs, while Table I illustrates the detailed eigenvalue analysis, with $U_{\text{f}}=0.3$ p.u.. In Fig. 6, the red triangles indicate the eigenvalues when the dynamic coupling effects are considered ($\lambda_{\text{c}j}$ and $\lambda_{\text{c}k}$), whereas the blue crosses indicate the eigenvalues without considering those effects ($\lambda_{\text{e}j}$ and $\lambda_{\text{e}k}$). As the fault location becomes farther away (R_{L} and X_{L} gradually become larger), the eigenvalues move in the directions of the arrows.

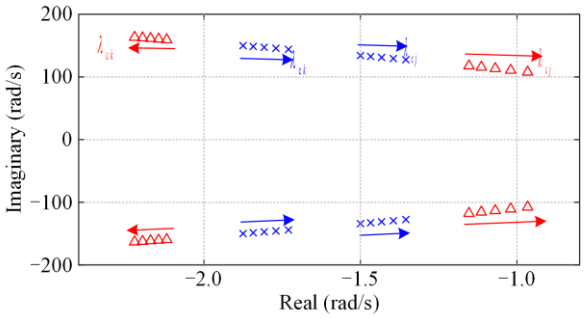

Fig. 6. Comparison of the eigenvalues trajectory of 2-WFs system when fault location becomes farther away.

TABLE I
EIGENVALUE ANALYSIS AS FAULT LOCATION BECOMES FARTHER AWAY

Z_L	Considering dynamic coupling	Eigenvalues	Damping ratio ξ
0.074 + j0.35	No	$\lambda_{oj} = -1.5 \pm j134.2$	0.0112
	Yes	$\lambda_{cj} = -1.153 \pm j117.6$	0.0098
	No	$\lambda_{ok} = -1.875 \pm j150$	0.0125
	Yes	$\lambda_{ck} = -2.119 \pm j159.4$	0.0133
0.092 + j0.434	No	$\lambda_{oj} = -1.355 \pm j127.5$	0.0106
	Yes	$\lambda_{cj} = -0.9661 \pm j107.7$	0.009
	No	$\lambda_{ok} = -1.73 \pm j144.1$	0.012
	Yes	$\lambda_{ck} = -2.211 \pm j162.5$	0.0136

From the above analysis, the dynamic coupling between the WFs will lead to the shift of the PLL-dominated poles of the two WFs. Specifically, it causes the PLL dominant poles of the *j*th and *k*th WFs to shift to the right and left, respectively. This suggests that the dynamic coupling effect between WFs introduces negative damping to the PLL-dominant modal of the WF located relatively far away from the fault location, while it adds positive damping to the PLL-dominant modal of the WF situated closer to the fault location. Moreover, as the fault location becomes farther away, the damping offset brought by the dynamic coupling effect to each WF's PLL-dominant modal become greater.

Figure 7 illustrates the motion trajectory of the PLL-dominant poles of the 2-WF system as the fault severity gradually increases, while Table II illustrates the detailed eigenvalue analysis. As can be seen, the damping shift brought by dynamic coupling between WFs to each WF become more obvious as the fault severity increases.

In simpler terms, when the farther fault location is farther away or the fault severity is greater, the dynamic coupling between WFs during LVRT is intensified. This heightened coupling also amplifies the damping offset that affects each WF.

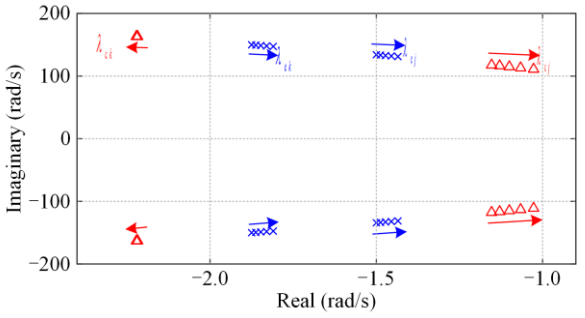

Fig. 7. Comparison of the eigenvalues trajectory of 2-WFs system when the fault severity increases.

TABLE II
EIGENVALUE ANALYSIS AS THE FAULT SEVERITY INCREASES

U_f	Considering dynamic coupling	Eigenvalues	Damping ratio ξ
0.32 p.u.	No	$\lambda_{oj} = -1.75 \pm j150$	0.0117
	Yes	$\lambda_{cj} = -1.185 \pm j122.1$	0.0097
	No	$\lambda_{ok} = -1.81 \pm j144.4$	0.0125
	Yes	$\lambda_{ck} = -2.218 \pm j163.1$	0.0136
0.11 p.u.	No	$\lambda_{oj} = -1.435 \pm j131.2$	0.0109
	Yes	$\lambda_{cj} = -1.027 \pm j111$	0.0093
	No	$\lambda_{ok} = -1.5 \pm j134.2$	0.0112
	Yes	$\lambda_{ck} = -2.222 \pm j163.3$	0.0136

B. Influence Mechanism of Dynamic Coupling on Small-signal Stability of n Multi-paralleled WFs System

In a system containing *n* multi-paralleled WFs, the dynamic coupling behavior within the system will be more complex during the LVRT. Figure 8 illustrates the dynamic interaction of *n* multi-paralleled WFs during LVRT.

It can be seen that each WF is dynamically coupled to the remaining *n*-1 WFs. In reality, the output currents and the control parameters of the *n* WFs during LVRT may be different, and therefore analyzing the dynamic stability and effect of dynamic coupling between WFs during LVRT becomes even more complicated. As seen in Fig. 8, $\boldsymbol{G}_n(s)$ is the transfer function of the *n*th WF's terminal voltage dynamic $\Delta U_{\mathrm{tq}}^{\mathrm{p}n}$ to its own PLL dynamics $\Delta\theta_{\mathrm{pll}n}$. $G_{jk}(s)$ is the transfer function from the *k*th WF's terminal voltage dynamic $\Delta U_{\mathrm{tq}}^{\mathrm{p}k}$ to the *j*th WF's PLL dynamic $\Delta\theta_{\mathrm{pll}j}$.

We assume that the PLL dominant poles of the independent *j*th DFIG WF is $-d_{jj} \pm \mathrm{j}k_{jj}$, while ΔD_{jk} represents the damping offset brought by the dynamic coupling between the *j*th and *k*th WFs on the PLL dominant poles of the *j*th WF. It can be seen that if the whole damping of the *j*th DFIG WF's PLL dominant poles in the multi-paralleled DFIG WFs system has $d_{jj} + \sum_{k=1,k\neq j}^{n} \Delta D_{jk} < 0$, this WF will experience small signal instability during LVRT.

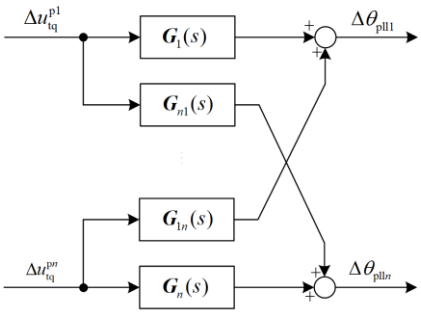

Fig. 8. Dynamic coupling relation of multi-paralleled WFs during LVRT.

In the following paragraphs, a system consisting of three DFIG WFs connected to the grid in parallel is used for analysis.

Figure 9 illustrates the motion trajectory of the PLL-dominant poles of the system containing three paralleled WFs as the fault location becomes farther away (R_{L} and X_{L} become larger), when the dynamic coupling effect is not considered. The detailed eigenvalues analysis is given in Table III, while the system parameters can be found in the Appendix A.

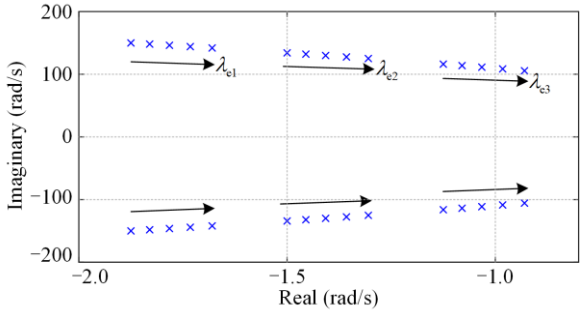

Fig. 9. Eigenvalue trajectory of the 3-WF system without considering dynamic coupling effects when the fault location becomes farther away.

As can be seen from Fig. 9 and Table III, without considering the dynamic coupling between WFs, the damping of each WF's PLL-dominant modal will decrease as the distance between the fault location and PCC increases. However, all the PLL dominant poles remain in the left half-plane of the complex plane.

TABLE III
EIGENVALUE ANALYSIS OF THE 3-WF SYSTEM DURING LVRT WITHOUT CONSIDERING DYNAMIC COUPLING EFFECTS

Z_{L}	WF	Eigenvalues	Damping ratio ξ
0.074 ± j0.35	1	−1.875 ± j150	0.0125
	2	−1.5 ± j134.2	0.0112
	3	−1.125 ± j116.2	0.0097
0.083 ± j0.392	1	−1.782 ± j146.2	0.0122
	2	−1.407 ± j130	0.0108
	3	−1.033 ± j111.3	0.0093
0.092 ± j0.434	1	−1.68 ± j142	0.0118
	2	−1.305 ± j125.1	0.0104
	3	−0.93 ± j105.6	0.0088

Figure 10 and Table IV respectively illustrate the motion trajectory and detailed eigenvalue analysis of the PLL-dominant poles in the three paralleled-connected DFIG WFs when the dynamic coupling effects between WFs during LVRT are considered.

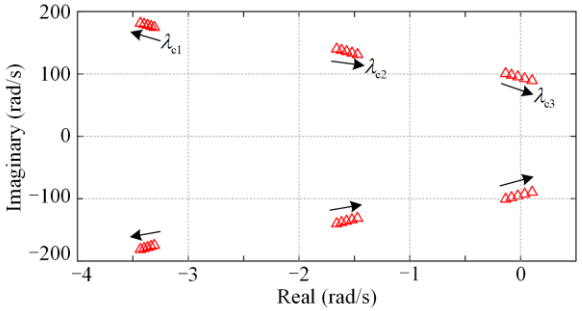

Fig. 10. Eigenvalue trajectory of the 3-WF system considering dynamic coupling effects when the fault location becomes farther away.

TABLE IV
EIGENVALUE ANALYSIS OF THE 3-WF SYSTEM DURING LVRT WITH CONSIDERING DYNAMIC COUPLING EFFECTS

Z_{L}	WF	Eigenvalues	Damping ratio ξ
0.074 ± j0.35	1	−3.306 ± j174.7	0.0189
	2	−1.66 ± j140	0.0119
	3	−1.351 ± j100.6	0.0013
0.083 ± j0.392	1	−3.367 ± j178.1	0.0188
	2	−1.571 ± j15.9	0.0116
	3	−0.02538 ± j95.48	0.0003
0.092 ± j0.434	1	−3.432 ± j181.3	0.0187
	2	−1.472 ± j131.2	0.0112
	3	0.1035 ± j89.4	−0.0012

It can be seen that the dynamic coupling between WFs during LVRT leads to damping shifts in the PLL-dominant modals of the system. Also, because of the dynamic coupling effect, the damping of the third DFIG WF becomes negative as the distance between the fault location and PCC increases, resulting in small-signal instability during LVRT.

Figure 11 and Table V respectively illustrate the motion trajectory and detailed eigenvalue analysis of the PLL-dominant poles in the system without considering the dynamic coupling effect between WFs, as the fault severity increases.

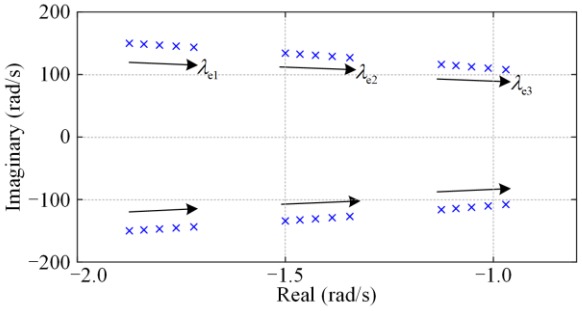

Fig. 11. Eigenvalue trajectory of the 3-WF system without considering dynamic coupling effects when fault severity increases.

TABLE V
EIGENVALUE ANALYSIS OF THE 3-WF SYSTEM DURING LVRT WITHOUT CONSIDERING DYNAMIC COUPLING EFFECTS

U_f	WF	Eigenvalues	Damping ratio ξ
0.32 p.u.	1	−1.845 ± j149.1	0.0124
	2	−1.455 ± j129.5	0.0112
	3	−1.089 ± j111.2	0.0097
0.22 p.u.	1	−1.802 ± j147.1	0.0122
	2	−1.427 ± j130.9	0.0109
	3	−1.053 ± j112.4	0.0094
0.11 p.u.	1	−1.72 ± j143.7	0.0120
	2	−1.345 ± j127	0.0106
	3	−0.97 ± j107.9	0.009

Figure 12 and Table VI respectively illustrate the motion trajectory and detailed eigenvalue analysis when the dynamic coupling effects between WFs are considered, as the fault severity increases.

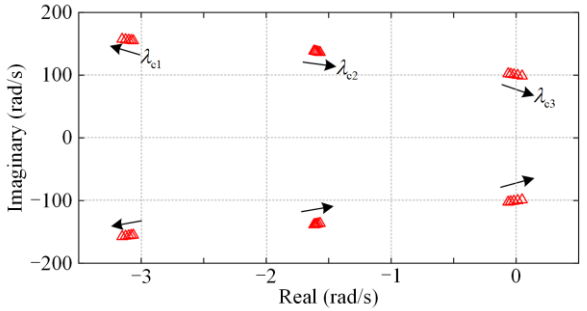

Fig. 12. Eigenvalue trajectory of the 3-WF system considering dynamic coupling effects when fault severity increases.

It can be seen that considering the dynamic coupling between WFs, the damping of each WF's PLL-dominant modal reduces as the fault severity increases. The dynamic coupling effect between WFs also causes the third WF's damping to become negative, resulting in small-signal instability during LVRT.

TABLE VI
EIGENVALUE ANALYSIS OF THE 3-WF SYSTEM DURING LVRT CONSIDERING DYNAMIC COUPLING EFFECTS

U_f	WF	Eigenvalues	Damping ratio ξ
0.32 p.u.	1	−3.064 ± j155	0.0198
	2	−1.618 ± j138.6	0.0117
	3	−0.06434 ± j102.4	0.0006
0.22 p.u.	1	−3.101 ± j156	0.0199
	2	−1.598 ± j137.6	0.0116
	3	−0.01824 ± j100.9	0.0002
0.11 p.u.	1	−3.153 ± j157.4	0.02
	2	−1.569 ± j136.3	0.0115
	3	0.04747 ± j98.75	−0.0005

In summary, the increase of distance between the fault location and PCC or the increase of fault severity is detrimental to the dynamic stability of the PLL-dominated multi-paralleled DFIG WFs during LVRT. There are two reasons for this:

1) The self-damping of the PLL dominant modal in each individual WF is reduced as the distance between the fault location and PCC increases or the fault severity becomes higher during LVRT.

2) The increase of distance between the fault location and PCC or the fault severity will amplify the dynamic coupling effects between WFs, which brings negative damping effects to certain WFs during LVRT.

IV. COOPERATIVE CONTROL FOR MULTI-PARALLELED DFIG WIND FARMS

The stability analysis reveals that the dynamic coupling between the WFs during the LVRT integrates multi-paralleled DFIG WFs into a unified system. The dynamic instability of any WF during LVRT will affect the stability of the overall system. To improve the dynamic stability, the damping of each independent WF should be enhanced, especially for WF with $-d_{jj} + \sum_{k=1,k\neq j}^{n} \Delta D_{jk}$ being less than zero or close to zero.

Here, an adaptive damping controller is designed for each ndividual WF, and its control structure is shown in Fig. 13. The adaptive damping controller directly feeds back the deviation between ω_{pll} and ω_{g} to the output of the q-axis GSC CCL through a PI controller, where k_{cp} and k_{ci} shown in Fig. 13 are the proportional and integral coefficients of the adaptive damping controller, respectively. In the case where ω_{pll} deviates from ω_{g} during LVRT, the DFIG WF will automatically adjust its q-axis current component according to $\Delta\omega_{\text{pll}}$.

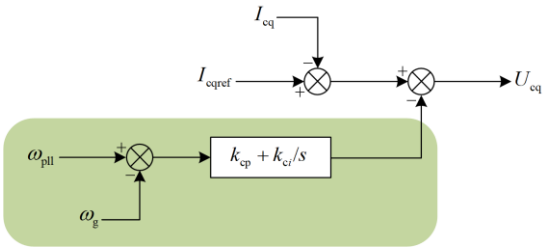

Fig. 13. Control structure of the adaptive damping controller.

After applying the adaptive damping controller, the damping ratio of an independent DFIG WF's PLL dominant mode changes from (9) to (10), as:

$$\xi = \frac{k_{\text{p}}}{2}\frac{U_{\text{td0}} - R_{\text{G}}I_{\text{gd0}} - X_{\text{G}}I_{\text{gq0}}}{\sqrt{k_{\text{i}}(U_{\text{td0}} - R_{\text{G}}I_{\text{gd0}} - X_{\text{G}}I_{\text{gq0}})}} \tag{9}$$

$$\xi^{*} = \frac{k_{\text{p}}}{2}\frac{U_{\text{td0}} - R_{\text{G}}I_{\text{gd0}} - X_{\text{G}}I_{\text{gq0}} + X_{\text{G}}K_{ci} + X_{\text{G}}\dfrac{k_{\text{i}}}{k_{\text{p}}}K_{\text{cp}}}{\sqrt{k_{\text{i}}(1 + X_{\text{G}}k_{\text{p}}K_{\text{cp}})(U_{\text{td0}} - R_{\text{G}}I_{\text{gd0}} - X_{\text{G}}I_{\text{gq0}} + X_{\text{G}}K_{ci})}} \tag{10}$$

It can be seen that the damping ratio of the independent WF during LVRT is affected by the adaptive

damping controller's control coefficients, and Fig. 14 shows its trend. As seen, the damping ratio ξ^* of the system is increased with the increase of k_{cp} and k_{ci} after applying the adaptive damping controller, and hence the dynamic stability of the DFIG WF during LVRT can be enhanced.

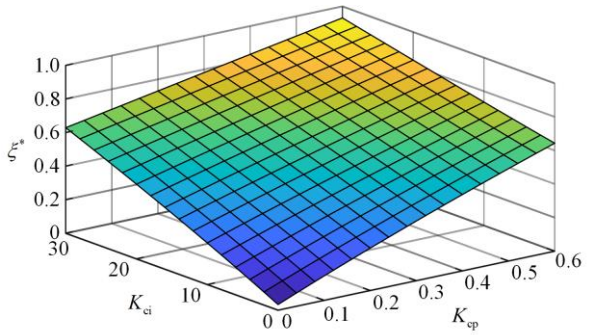

Fig. 14. Change trend of ξ^* with the change of k_{cp} and k_{ci}.

However, the multi-paralleled DFIG WFs constitute a coupled MIMO system, with dynamic coupling between each independent WF. We assume that the damping ratio of the *j*th WF is increased to the target value by adjusting its adaptive damping controller parameters. However, when the coefficients of the remaining $n-1$ WFs are subsequently adjusted, the changes of the states of the remaining $n-1$ WFs will inevitably influence the damping of the *j*th WF through dynamic coupling.

The PLL dominant poles of the 3rd and 4th WF in a 5-WF grid-connected system are given in Fig. 15. In the initial state of Fig. 15, the 3rd WF has been regulated to be dynamically stable but the 4th WF has not yet been regulated. Then, the adaptive damping controller is added to the 4th WF and is adjusted to make it dynamically stable during the LVRT. The poles move according to the orientations of the arrows as shown in Fig. 15.

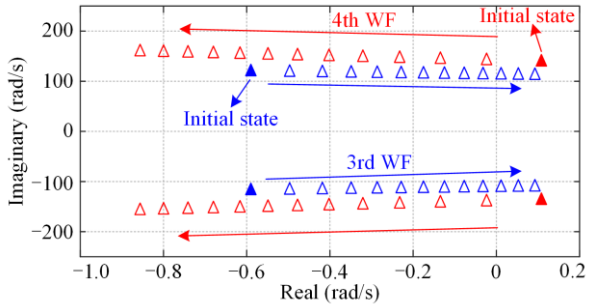

Fig. 15. Eigenvalue trajectory of the 3rd and 4th WFs in a 5-WF system as adjusting adaptive damping controller in the 4th WF.

It can be seen that the PLL dominant poles of the 4th WF are shifted to the left and the system tends to be dynamically stable. However, because of the dynamic coupling between the WFs, adjusting the 4th WF's parameters also influences the 3rd WF. As a result, the PLL dominant poles of the 3rd WF shifts to the right, thus making the 3rd WF dynamically unstable. Therefore, it is not feasible to independently adjust the parameters of the adaptive damping controller applied in each WF.

In the proposed cooperative control strategy, each DFIG WF will adopt the adaptive damping controller in Fig. 13, while the adaptive damping controller's coefficients for each WF will be configured considering the state of the overall system during LVRT. Thus, the damping of each subsystem is changed to ensure overall system stability. The basic procedure of the cooperative control strategy is as follows:

1) Combined with the actual system, establish the small-signal state space equations of the overall WF system under symmetric faults. Calculate the range of fault distance and fault severity which can lead to small signal instability during LVRT.

2) Establish the time-domain simulation model of the *n* multi-paralleled DFIG WF grid-connected system, and simulate the typical symmetric voltage dip faults in the calculated range, combined with the actual situation (including different fault locations and fault severities).

In the 3-WF system in Section III, the calculated range of fault distance and fault severity which will lead to dynamic instability are: $\boldsymbol{Z}_L$ is larger than $0.087 + \mathrm{j}0.411$ p.u., and U_f is lower than 0.2 p.u. So every $0.001 + \mathrm{j}0.0047$ p.u. increase in $\boldsymbol{Z}_L$ or every 0.01 p.u. decrease in U_f is a selected fault scenario in the system.

3) When a fault occurs, calculate the PLL dominant poles in the system and the damping ratio ξ^* of each WF.

4) Judge whether the real parts of the *n* PLL dominant poles are all negative and the damping ratios satisfy the set target value. If all conditions are satisfied, go to step 6. Otherwise, go to step 5.

5) If the conditions of step (4) are unsatisfied, determine the target-unsatisfied WF's sequence and modify the parameters of its adopted adaptive damping controller according to (10) and Fig. 17. Subsequently, update the model parameters and go back to step (2).

6) If the conditions of step (4) are all satisfied, the iteration will stop and the optimal solution will be generated. Enter the simulation model to verify.

7) Store the fault data and control data in the centralized control system. Change the fault scenario and recalculate the new control data until all fault scenarios have been calculated.

8) When a voltage dip is detected in the actual grid-connected system, the fault information will be obtained by the centralized control system [24]. A similar fault scenario will be identified in the system, and the control data for this scenario will be issued to the corresponding WF. The whole process of the cooperative control strategy is shown in Fig. 16.

The process in the blue part in Fig. 16 corresponds to steps (1) to (6).

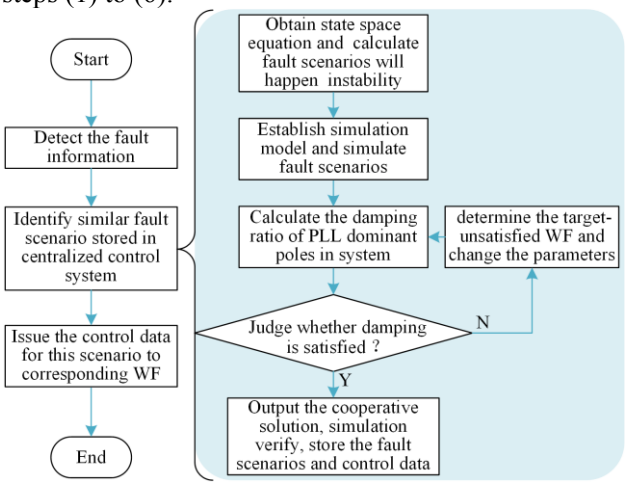

Fig. 16. Process of the cooperative control strategy.

These steps are actually carried out when the WFs are being installed, and the data are stored in the centralized control system [24]. When a voltage dip is detected in the actual grid-connected system, only the steps on the left part in Fig. 16 need to be performed. Since the communication technology represented by Ethernet communication is applied in the control of WFs [25], the command sending and receiving time can generally be controlled within 10 ms [26]. This meets the time requirements of fault ride-through operation.

The motion trajectories of the PLL-dominated poles for different fault distance and fault severity in the multi-paralleled DFIG WFs after applying the cooperative control are given in Figs. 17 (a) and (b), respectively.

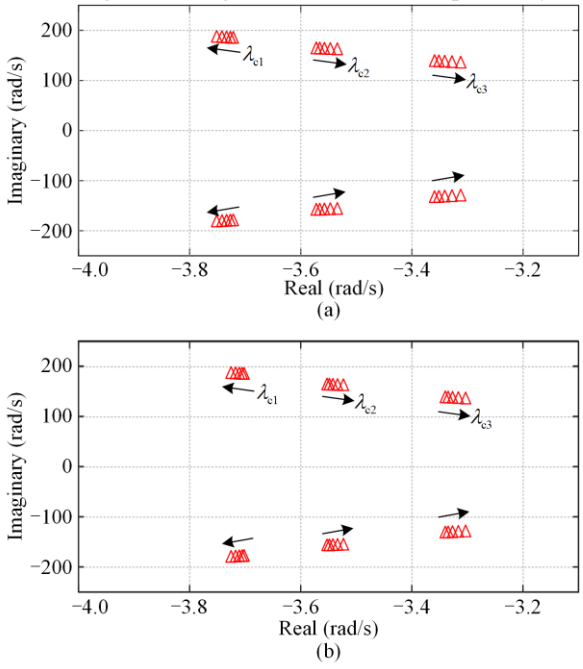

Fig. 17. Eigenvalue trajectory of the 3-WF system after applying the cooperative control. (a) When fault location becomes farther away. (b) When fault becomes more severe.

As seen in Fig. 17, with the application of the cooperative control strategy, each WF can ensure dynamic stability during the LVRT, regardless of fault location or severity.

V. Simulation Validation

To verify the correctness of the above analysis and the effectiveness of the proposed cooperative control strategy on dynamic stability improvement during LVRT, a multi-paralleled WF system model is established in MATLAB/Simulink. This consists of three DFIG WFs as shown in Fig. 18. The parameters of the WFs and lines are referenced from a multi-paralleled WF system in the Baotou area of China. The DFIG WFs are connected to the PCC through step-up transformers, and then connected to the grid through the common transmission line $\boldsymbol{Z}_{\mathrm{L}}$ and additional step-up transformers. Grid faults occur at the fault point on the high-voltage cable [27]. The detailed parameters of the system are given in the Appendix A.

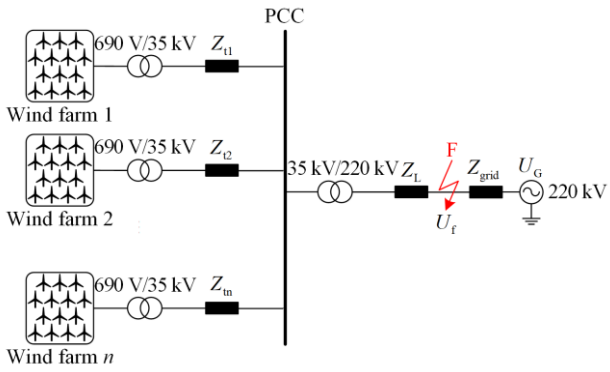

Fig. 18. Structure of the simulation model of a multi-paralleled WF system.

A. Simulation Validation for the Influence of Dynamic coupling between WFs

Figure 19 shows the simulation results without applying the cooperative control strategy, when $\boldsymbol{Z}_{\mathrm{L}} = 0.0875 + j0.413$ p.u. . As can be seen, the third WF experiences small signal instability during the LVRT. Because of the dynamic coupling between the WFs, the terminal dynamics of the WFs influence each other during the LVRT.

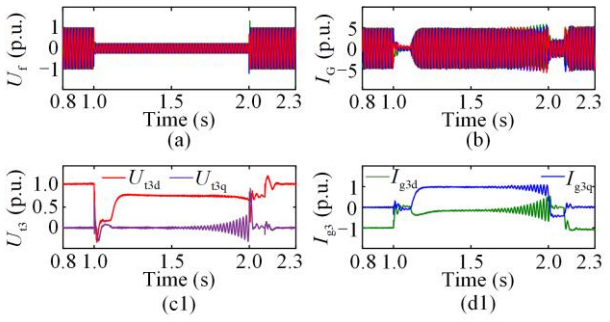

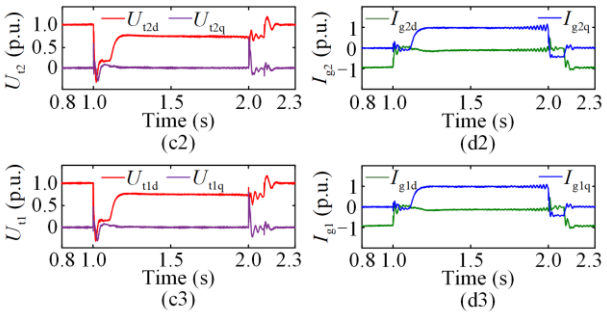

Fig. 19. Simulation results when $Z_{\mathrm{L}} = 0.0875 + \mathrm{j}0.413$ p.u. (a) Three-phase voltage of fault point. (b) Three-phase current of PCC. (c1)–(c3) The *dq* components of terminal voltages of the 3rd, 2nd and 1st WFs respectively. (d1)–(d3) The *dq* components of terminal currents of the 3rd, 2nd and 1st WFs respectively.

To verify the influence of dynamic coupling between WFs on the dynamic stability of the multi-paralleled WF system during LVRT, three independent wind farms are established, as shown in Fig. 20. These three WFs are connected to the grid independently. The rest of the parameters and control structures are the same as in the model of Fig. 18, with $Z_{\mathrm{L1}} = Z_{\mathrm{L2}} = Z_{\mathrm{L3}} = Z_{\mathrm{L}}$, $Z_{\mathrm{grid1}} = Z_{\mathrm{grid2}} = Z_{\mathrm{grid3}} = Z_{\mathrm{grid}}$, $U_{\mathrm{G1}} = U_{\mathrm{G2}} = U_{\mathrm{G3}} = U_{\mathrm{G}}$.

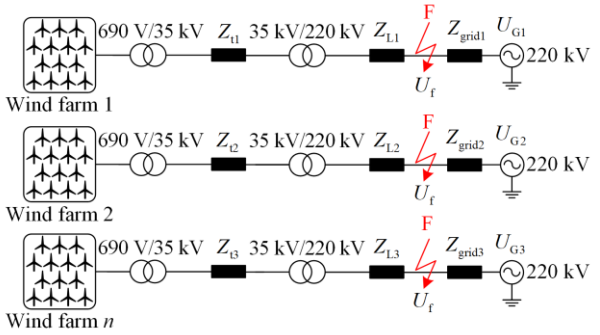

Fig. 20. Structure of a three independent wind farm system.

The simulation results for the three independent DFIG WFs during LVRT are given in Fig. 21.

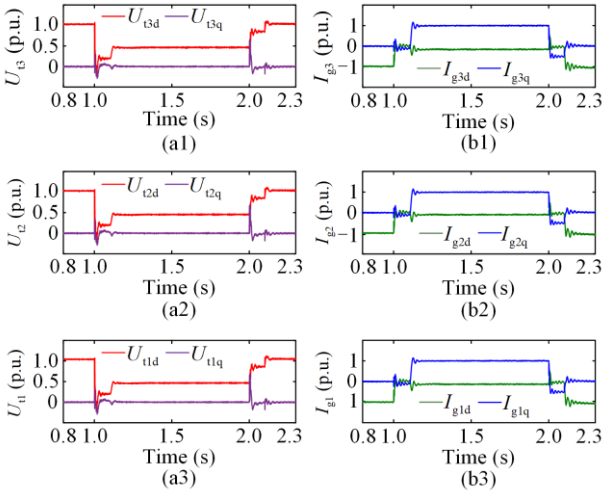

Fig. 21. Simulation results without considering dynamic coupling during LVRT. (a1)–(a3) The *dq* components of terminal voltages of 3rd, 2nd and 1st WFs respectively. (b1) –(b3) The *dq* components of terminal currents of 3rd, 2nd and 1st WFs respectively.

It can be seen that the three independent WFs can all remain stable during LVRT when there is no dynamic coupling between them. Comparing Figs. 19 and 21, the analysis in Tables III and Table IV can be verified, i.e., the dynamic coupling between WFs is the important cause of small-signal instability during LVRT of the multi-paralleled WF system.

B. Simulation Validation for the Influence of Fault Location and Fault Degree

Figure 22 shows the simulation results without applying the cooperative control strategy, when the distance to fault location becomes farther away to $Z_{\mathrm{L}} = 0.092 + \mathrm{j}0.434$ p.u.

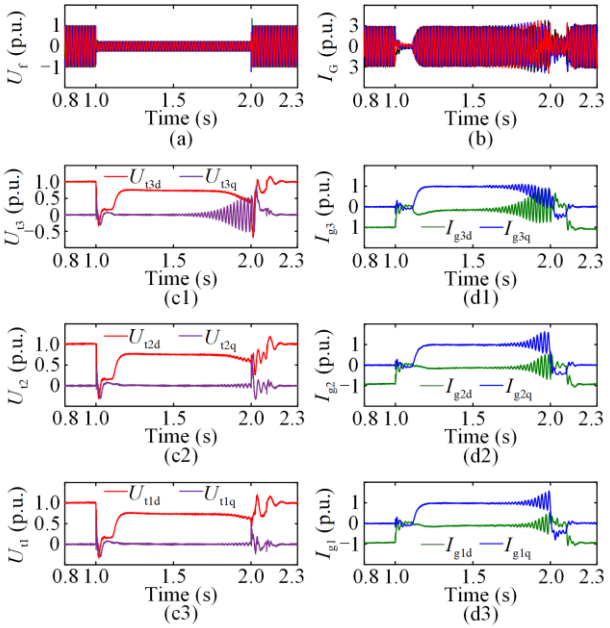

Fig. 22. Simulation results when $Z_{\mathrm{L}} = 0.092 + \mathrm{j}0.434$ p.u. (a) Three-phase voltage of fault point. (b) Three-phase current of PCC. (c1)–(c3). The *dq* components of terminal voltages of 3rd, 2nd and 1st WFs respectively. (d1)–(d3) The *dq* components of terminal currents of 3rd, 2nd and 1st WFs respectively.

Comparing the simulation results in Figs. 19 and 22, as the distance to fault location becomes farther away, the multi-paralleled WF system becomes more unstable during LVRT and the small-signal instability phenomenon worsens. The THD of the phase-a terminal voltages of the 1st, 2nd and 3rd WFs rise from 4.11%, 4.54%, and 19.98% to 15.5%, 21.11%, and 38%, respectively. The small signal instability in the third WF also leads to small signal instability in the other WFs because of the dynamic coupling between the WFs during LVRT.

Figure 23 shows the simulation results without applying the cooperative control strategy, when the fault severity increases to $U_{\mathrm{f}} = 0.1$ p.u. .

Comparing the simulation results in Figs. 19 and 23, as the fault severity increases, the THD of the phase-a terminal voltages of the 1st, 2nd and 3rd WFs rise to

9.82%, 17.67%, and 29.15%, respectively. In addition, the increase of the fault severity makes the system more unstable.

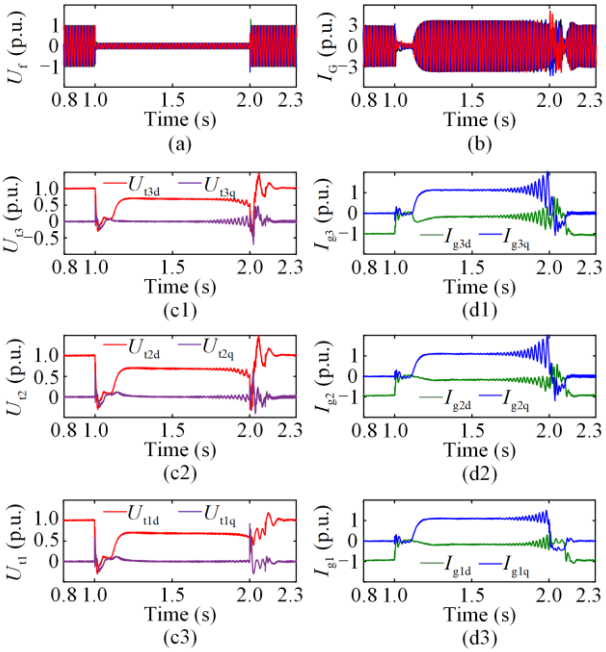

Fig. 23. Simulation results when $U_f = 0.1$ p.u. (a) Three-phase voltage of fault point. (b) Three-phase current of PCC. (c1)–(c3) The *dq* components of terminal voltages and currents of 3rd, 2nd and 1st WFs respectively. (d1)–(d3) The *dq* components of terminal currents of 3rd, 2nd and 1st WFs respectively.

The simulation results show that when the distance between the fault location and PCC becomes longer or the fault severity increases, the dynamic stability of the multi-paralleled DFIG WF system during LVRT gradually deteriorates. Moreover, because of the dynamic coupling effect between WFs, a WF which incurs dynamic instability can induce small signal instability in other WFs during LVRT. This confirms the analysis in this paper.

C. Simulation Validation for Effectiveness of the Proposed Cooperative Control Strategy

In Fig. 24, the cooperative control strategy is applied and $\boldsymbol{Z}_L = 0.092 + \mathrm{j}0.434$ p.u. It can be seen that the dynamic stability of the multi-paralleled WFs during the LVRT is improved and small-signal instability is avoided.

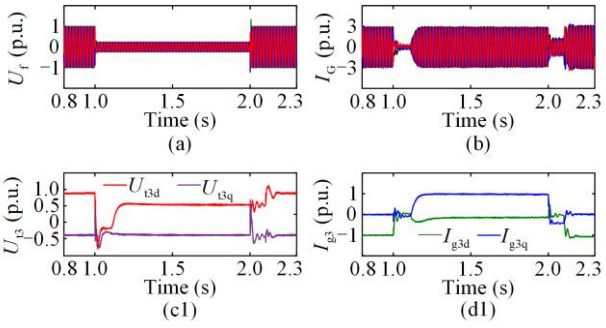

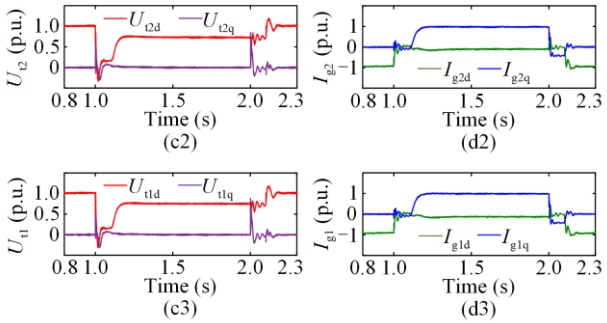

Fig. 24. Simulation results with applying cooperative control strategy and $\boldsymbol{Z}_L = 0.092 + \mathrm{j}0.434$ p.u. (a) Three-phase voltage of fault point. (b) Three-phase current of PCC. (c1)–(c3) The *dq* components of terminal voltages of 3rd, 2nd and 1st WFs respectively. (d1)–(d3) The *dq* components of terminal currents of 3rd, 2nd and 1st WFs respectively.

Figure 25 shows the simulation results when the cooperative control strategy is applied, with $U_f = 0.1$ p.u. As seen, after applying the cooperative control strategy, the dynamic stability of the system during LVRT is enhanced and small-signal instability is avoided.

The simulation results in Figs. 24 and 25 verify the analysis in Fig. 17 that the proposed cooperative control strategy can ensure the stability of the whole system during LVRT. The simulation results after applying the proposed cooperative control strategy prove the effectiveness of the proposed cooperative control strategy on the dynamic stability improvement of a multi-paralleled WF system during LVRT.

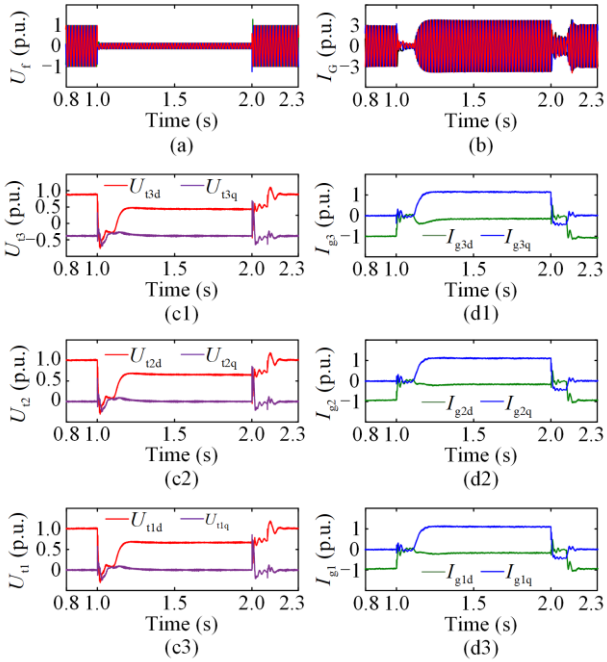

Fig. 25. Simulation results with applying cooperative control strategy and $U_f = 0.1$ p.u. (a) Three-phase voltage of fault point. (b) Three-phase current of PCC. (c1)–(c3) The *dq* components of terminal voltages of 3rd, 2nd and 1st WFs respectively. (d1)–(d3) The *dq* components of terminal currents of 3rd, 2nd and 1st WFs respectively.

VI. Conclusion

In this study, the mechanism and influence of dynamic coupling between multi-paralleled DFIG wind farms during fault steady-state of LVRT is investigated. Also, a cooperative control strategy is proposed to improve the system's dynamic stability during LVRT. The main conclusions are:

1) During the fault steady-state of a symmetrical voltage dip, there is a dynamic coupling effect between multi-paralleled WFs, caused by the dynamic interaction between each WF's output current and the PCC voltage. In addition, the dynamic coupling between WFs will bring a damping shift to each WF during LVRT, which in turn affects the small-signal stability of the system during the fault steady-state.

2) The distance between the fault location and PCC becoming farther away or the increase in fault severity will exacerbate the dynamic coupling between WFs. Moreover, increased distance from fault location and fault severity will lead to a reduction in WF self-damping. When the sum of the certain WF's self-damping and the damping offset caused by dynamic coupling is negative, the WF becomes dynamically unstable during LVRT.

3) The dynamic coupling between the WFs during LVRT integrates multi-paralleled DFIG WFs into a unified system, and adjusting the control state of any WF will affect the stability of the remaining WFs in the multi-fed system. The proposed cooperative control strategy adjusts the damping of the entire system and thus improves the system's dynamic stability during LVRT. The simulation verifies the effectiveness of the proposed strategy.

Because there is currently a lack of an experimental platform for multi-WF grid-connected system, this paper uses modal computation and simulation to verify the developed control strategy. The parameters of the simulation system are set according to WFs in an actual project to ensure the accuracy of the verification process. We are presently developing the multi-fed grid-connected experimental platform, and consequently, the findings of this study will be subjected to validation on this experimental platform in the future.

Appendix A

A. Simulation Parameters

TABLE A1
Parameters of the DFIG Wind Farms

Parameter	Value	Parameter	Value
P_{rated}	200 MW	U_{rated}	690 V
f	50 Hz	R_s	0.02 p.u.
L_s	0.17 p.u.	R_r	0.017 p.u.
L_r	0.17 p.u.	L_m	2.8 p.u.
R_{t1}	0.029 p.u.	R_{t2}	0.037 p.u.
X_{t1}	0.141 p.u.	X_{t2}	0.189 p.u.
R_{t3}	0.044 p.u.	X_{t3}	0.239 p.u.

Acknowledgment

Not applicable.

Authors' Contributions

Lei Guan: model the system, analyze, design the algorithm of control strategy, and write the paper. Jun Yao: put forward the initial concept and give technical guidance in the whole process, and contribute to the revision and typesetting of the manuscript. All authors read and approved the final manuscript.

Funding

This work is supported in part by the National Natural Science Foundation of China (NSFC) (No. 51977019), and in part by the Joint Research Fund in Smart Grid under Cooperative Agreement between the National Natural Science Foundation of China (NSFC) (No. U1966208), and State Grid Corporation of China (SGCC).

Availability of Data and Materials

Not applicable.

Declarations

Competing interests: The authors declare that they have no known competing financial interests or personal relationships that could have appeared to influence the work reported in this article.

Authors' Information

Lei Guan received the B.Eng. degree in automation from Huazhong University of Science and Technology Wuchang Branch, Wuhan, China, in 2014 and the M.Sc. degree in control science and engineering from Anhui University, Hefei, China, in 2017. He is currently working toward the Ph.D. degree in the College of Electrical Engineering at Chongqing University, Chongqing, China. His research interests include electric machines control, modelling and control of wind turbine generation system, and renewable power generation.

Jun Yao received the B.Eng., M.Sc., and Ph.D. degrees from Chongqing University, Chongqing, China, in 2001, 2004, and 2007, respectively, all in electrical engineering. Since 2004, he has been with the School of Electrical Engineering, Chongqing University, where he is currently a professor. He was a visiting researcher at the Department of Energy Technology, Aalborg University, Aalborg, Denmark, from January 2012 to January 2013. He is a member of IEC SC8A JWG5. He is the author/coauthor of more than 100 peer-reviewed technical papers, and holds more than 20 issued/pending patents. His research interests include electric machines

control, power electronics conversion and control, and renewable power generation; and his main current research interests are wind energy and power electronics application to the power systems.

REFERENCES

[1] T. S. L.V. Ayyarao, "Modified vector controlled DFIG wind energy system based on barrier function adaptive sliding mode control," *Protection and Control of Modern Power Systems*, vol. 4, no. 1, pp. 34-41, Jan. 2019.

[2] S. Mokred, Y. Wang, and T. Chen, "A novel collapse prediction index for voltage stability analysis and contingency ranking in power systems," *Protection and Control of Modern Power Systems*, vol. 8, no. 1, pp. 112-138, Jan. 2023.

[3] Y. Yang, D. Zhu, and D. Zhou *et al*., "Synchronization instability mechanism and damping enhancement control for DFIG-based wind turbine during grid faults," *IEEE Transactions on Power Electronics*, vol. 38, no. 10, pp. 12104-12115, Oct. 2023.

[4] R. Babu, S. Raj, and B. Bhattacharyya, "Weak bus-constrained PMU placement for complete observability of a connected power network considering voltage stability indices," *Protection and Control of Modern Power Systems*, vol. 5, no. 4, pp. 294-307, Oct. 2020.

[5] G. Pannell, D. J. Atkinson, and B. Zahawi, "Minimum-threshold crowbar for a fault-ride-through grid-code-compliant DFIG wind turbine," *IEEE Transactions on Energy Conversion*, vol. 25, no. 3, pp. 750-759, Sept. 2010.

[6] Z. Tian, X. Li, and X. Zha *et al*., "Transient synchronization stability of an islanded AC microgrid considering interactions between grid-forming and grid-following converters," *IEEE Journal of Emerging and Selected Topics in Power Electronics*, vol. 11, no. 4, pp. 4463-4476, Aug. 2023.

[7] M. G. Taul, X. Wang, and P. Davari *et al*., "An overview of assessment methods for synchronization stability of grid-connected converters under severe symmetrical grid faults," *IEEE Transactions on Power Electronics*, vol. 34, no. 10, pp. 9655-9670, Oct. 2019.

[8] R. Liu, J. Yao, and X. Wang *et al*., "Dynamic stability analysis and improved LVRT schemes of DFIG-based wind turbines during a symmetrical fault in a weak grid," *IEEE Transactions on Power Electronics*, vol. 35, no. 1, pp. 303-318, Jan. 2020.

[9] J. Hu, B. Wang, and W. Wang *et al*., "Small signal dynamics of DFIG-based wind turbines during riding through symmetrical faults in weak AC grid," *IEEE Transactions on Energy Conversion*, vol. 32, no. 2, pp. 720-730, Jun. 2017.

[10] J. Hu, Q. Hu, and B. Wang *et al*., "Small signal instability of PLL-synchronized type-4 wind turbines connected to high-impedance AC grid during LVRT," *IEEE Transactions on Energy Conversion*, vol. 31, no. 4, pp. 1676-1687, Dec. 2016.

[11] X. Fang, J. Yao, and R. Liu *et al*., "Small-signal stability analysis and current control reference optimization algorithm of DFIG-based WT during asymmetric grid faults," *IEEE Transactions on Power Electronics*, vol. 36, no. 7, pp. 7750-7768, Jul. 2021.

[12] W. Du, W. Dong, and H. Wang *et al*., "Dynamic aggregation of same wind turbine generators in parallel connection for studying oscillation stability of a wind farm," *IEEE Transactions on Power Systems*, vol. 34, no. 6, pp. 4694-4705, Nov. 2019.

[13] W. Li, A. M. Gole, and I. Kaffashan *et al*., "Structure preserving aggregation method for doubly-fed induction generators in wind power conversion," *IEEE Transactions on Energy Conversion*, vol. 37, no. 2, pp. 935-946, Jun. 2022.

[14] W. Zhai, Q. Jia and G. Yan, "Analysis of sub synchronous oscillation characteristics from a direct drive wind farm based on the complex torque coefficient method," *CSEE Journal of Power and Energy Systems*, pp. 1-10, doi: 10.17775/CSEEJPES.2021.05760.

[15] W. Dong, H. Xin, and D. Wu *et al*., "Small signal stability analysis of multi-infeed power electronic systems based on grid strength assessment," *IEEE Transactions on Power Systems*, vol. 34, no. 2, pp. 1393-1403, Mar. 2019.

[16] X. He and H. Geng, "PLL synchronization stability of grid-connected multi converter systems," *IEEE Transactions on Industry Applications*, vol. 58, no. 1, pp. 830-842, Jan.-Feb. 2022.

[17] S. Chen, J. Yao, and Y. Liu *et al*., "Coupling mechanism analysis and transient stability assessment for multiparalleled wind farms during LVRT," *IEEE Transactions on Sustainable Energy*, vol. 12, no. 4, pp. 2132-2145, Oct. 2021.

[18] P. Wang, Z. Zhang, and C. Chen *et al*., "Multistage parameter identification featured generic wind farm dynamic equivalent modeling," *IEEE Transactions on Industry Applications*, pp. 1-10. doi: 10.1109/TIA.2023.3307656.

[19] P. Sun, H. Xu, and J. Yao, *et al*., "Dynamic interaction analysis and damping control strategy of hybrid system with grid-forming and grid-following control modes," *IEEE Transactions on Energy Conversions*, vol. 38, no. 3, pp. 1639-1649, Sept. 2023.

[20] "Technical rule for connecting wind farm to power system," Chinese Standard: GB/T 19963-2011, China Electric Power Press, Beijing, China, 2011.

[21] W. Du, W. Dong and H. F. Wang, "Small-signal stability limit of a grid-connected PMSG wind farm dominated by the dynamics of PLLs," *IEEE Transactions on Power Systems*, vol. 35, no. 3, pp. 2093-2107, May 2020.

[22] N. Verma, N. Kumar, and S. Gupta *et al*., "Review of sub-synchronous interaction in wind integrated power systems: classification, challenges, and mitigation techniques," *Protection and Control of Modern Power Systems*, vol. 8, no. 2, pp. 277-302, Apr. 2023.

[23] C. Wang, Z. Wang, and Q. Wu *et al*., "An improved impedance/admittance analysis method considering collector subsystem transformation in converter-integrated power systems," *IEEE Transactions on Power Systems*, vol. 36, no. 6, pp. 5963-5966, Nov. 2021.

[24] Z. Gao, J. Geng, and K. Zhang *et al*., "Wind power dispatch supporting technologies and its implementation," *IEEE Transactions on Smart Grid*, vol. 4, no. 3, pp. 1684-1691, Sept. 2013.

[25] X. Yin, Y. Tan, and M. Bai *et al*., "Remote centralized control scheme for wind farms," in *2017 International*

Conf. Computer Technology, Electronics and Communication (ICCTEC), Dalian, China, Dec. 2017, pp. 960-963.

[26] S. Hussain, Y. C. Kim, and Q. Jan *et al*., "Simulation studies of reconfigurable communication network for southwest offshore wind farm South Korea," in *2019 International Conference Communication, Computing and Digital Systems (C-CODE)*, 2019, pp. 58-63.

[27] A. S. L. V. Tummala, "A robust composite wide area control of a DFIG wind energy system for damping inter-area oscillations," *Protection and Control of Modern Power Systems*, vol. 5, no. 3, pp. 260-269, Jul. 2020.

[28] U. Buragohain and N. Senroy, "Reduced order DFIG models for PLL-based grid synchronization stability assessment," *IEEE Transactions on Power Systems*, vol. 38, no. 5, pp. 4628-4639, Sept. 2023.

[29] Z. Zhang, X. Zhao, and L. Fu *et al*., "Stability and dynamic analysis of the PMSG-based WECS with torsional oscillation and power oscillation damping capabilities," *IEEE Transactions on Sustainable Energy*, vol. 13, no. 4, pp. 2196-2210, Oct. 2022.